Supplement of

Measurement report: Six-year DOAS observations reveal post-2020 rebound of ship SO_2 emissions in a Shanghai port despite low-sulfur fuel policies

Jiaqi Liu et al.

Correspondence to: Bin zhou (binzhou@fudan.edu.cn) and Shanshan Wang (shanshanwang@fudan.edu.cn)

Text S1. DOAS measurements and spectral data processing.

The active DOAS system for measuring SO_2 in Wusong Warf (WSW) is placed in the Wusong Maritime Safety Administration and the opposite of Huangpu River (the arrow of reflection mirror). While the system for Fudan University (FDU) is the Environmental Science Building and the southwest corner of campus (the arrow of reflection mirror). Both systems equipped with a 150 W Xenon lamp (Hamamatsu Photonics (China) Co., Ltd) and spectrometers (B&W Tek) with wavelength ranges of 185~440 nm. WSW's DOAS equipment can also observe the concentration changes of NO_2, HONO, O_3 and HCHO in the channel. To eliminate the effect of dark currents and atmospheric scattering light on the measurement, we subtracted the background spectrum collected by blocking the lamp's emitted light from the normally collected spectrum during the measurement spectrum sampling period. The average time resolution was 5~6 min for FDU's systems and 1~2 min for WSW's system. The observation site characteristics and the experimental setup for SO_2, NO_2, HONO, HCHO and O_3 measurements have been described in detail in previous studies (Guo et al., 2020; Liu et al., 2024).

The principle of DOAS is to utilize the narrow-band absorption characteristics of trace gases to determine the gas composition and to infer the concentration of trace gases. DOAS measurements of SO_2 have been mentioned in many studies and is a mature monitoring and analysis method (Cheng et al., 2019; Jin et al., 2016; Wang et al., 2019). In this study, the absorption cross sections of SO_2 (Voigt et al., 2002), HCHO, NO_2, O_3 and the solar spectrum were involved in SO_2 spectral fitting, using wavelength range of 299~308 nm. Based on the signal-to-noise ratio at a given optical path length and integration time, the detection limit in WSW is about 0.13 ppbv for SO_2, 0.51 ppbv for NO_2, 2.51 ppbv for O_3, 1.10 ppbv for HCHO, respectively. While the detection limit for SO_2 in FDU is 0.11 ppbv. The spectral fitting information of all the trace gas can be referred to **Table S1**.

Table S1. The detection limits of DOAS retrieval and the analytical residual.

Observed Station	Trace gas	Fitting window (nm)	absorption cross sections	Polynomial degree	Detection limits	Residuals
WSW	SO_2	299~308	SO_2 (Vandaele et al., 1998),NO_2 (Voigt et al., 2002), HONO (Stutz et al., 2000), HCHO (Meller and Moortgat, 2000), and solar spectrum (Kurucz, 1984)	5	0.13 ppbv	0.00054
	NO_2	365.3-380.4	NO_2 (Voigt et al., 2002), HONO (Stutz et al., 2000), HCHO (Meller and Moortgat, 2000), and solar spectrum (Kurucz, 1984)	5	0.51 ppbv	0.00043
	O_3	280.6-290.6	O_3 (Voigt et al., 2001a; Voigt et al., 2001b) , SO_2(Vandaele et al., 1998), HCHO (Meller and Moortgat, 2000), and NO_2 (Voigt et al., 2002)	5	2.51 ppbv	0.00154

	HCHO	313~341	HCHO (Meller and Moortgat, 2000), NO_2 (Voigt et al., 2002), SO_2(Vandaele et al.,1998), O_3 (Voigt et al., 2001a), HONO(Stutz et al.,2000)	5	1.10 ppbv	0.00057
FDU	SO_2	299~308	SO_2 (Vandaele et al., 1998),NO_2 (Voigt et al., 2002), HONO (Stutz et al., 2000), HCHO (Meller and Moortgat, 2000), and solar spectrum (Kurucz, 1984)	5	0.11 ppbv	0.00045

Text S2. Machine learning data input, model tuning, and performance evaluation.

We selected eight representative models as candidates, including one non-ensemble algorithms DecisionTreeRegressor (DTR), and seven ensemble models of ExtraTreeRegressor (ETR), RandomForestRegressor (RF), GradientBoostingRegressor (GBR), BaggingRegressor (BR), AdaBoostRegressor (ABR), XGBRegressor (XGB) and LGBMRegressor (LGBR). Those above algorithms are integrated in SCIKIT-LEARN (sklearn), an open-source machine learning library written in PYTHON (Hackeling, 2017). After performing grid search and 5-fold cross-validation, XGB and ETR were selected as models for filling missing date and de-meteorologizing according to their Root Mean Squared Error (RMSE) and Coefficient of Determination (R^2).

XGB is an optimized distributed gradient enhancement library designed for efficiency, flexibility, and portability. It implements machine learning algorithms in the Gradient Boosting framework. Gradient Boosting, proposed by Friedman [2001], is a large class of algorithms in Boosting. Its idea is borrowed from gradient descent, and its basic principle is to train newly added weak learners based on the negative gradient information of the loss function of the current model and then combine the trained learners into the existing model in an accumulative form. The ETR model not only randomly selects data samples when constructing each decision tree, but also randomly selects eigenvalues to be partitioned when the nodes split. This extreme randomness reduces the variance of the model, thus obtaining a better ability to reduce overfitting and improve model stability than Random Forest models (Gall et al., 2011).

When training the model to fill the missing SO_2 values at FDU, seven meteorological data (from ERA5), time-series NO_2 concentration data observed by DOAS at FDU (representing the emission trends most closely associated with SO_2 variations within the FDU campus environment), and SO_2 data from two nearby stations, Hongkou Station and Ynagpu Station, during the same period (providing a macroscopic perspective of SO_2 variation across Shanghai's land areas) were utilized. With model R^2 is 0.86, RMSE is 0.42 ± 0.13.

When training the model to fill the missing SO_2 values at WSW, seven meteorological data (from ERA5), other pollutant data observed by DOAS at WSW (including HCHO, O_3, and NO_2, used to characterize the environmental features of the shipping channel), and Deweathered_FDU (used to represent the variation in land-based SO_2

emissions within the urban environment) were utilized. With model R^2 is 0.76, RMSE is 0.65±0.21. The SO_2 concentration after completion is shown in **Figure S1**.

Deweathered models used seven meteorological data (from ERA5) and time-related variables (Unix time, Julian day, and day of the week) to capture emission patterns. ERA5 meteorological data from the same hour within 14 days before and after each target time was used, providing 1,276 sets of meteorological data for training on the Observed_WSW and Observed_FDU series, as showed in **Figure S2**. The repeated input of over 1,000 sets of real historical meteorological data can be considered sufficient to effectively account for the impacts of various real-world meteorological conditions. For the Deweathered models constructed for both WSW and FDU, the RMSE, R^2, are reported as 0.41±0.12 and 0.79 in WSW, 0.32±0.14 and 0.85 in FDU, respectively.

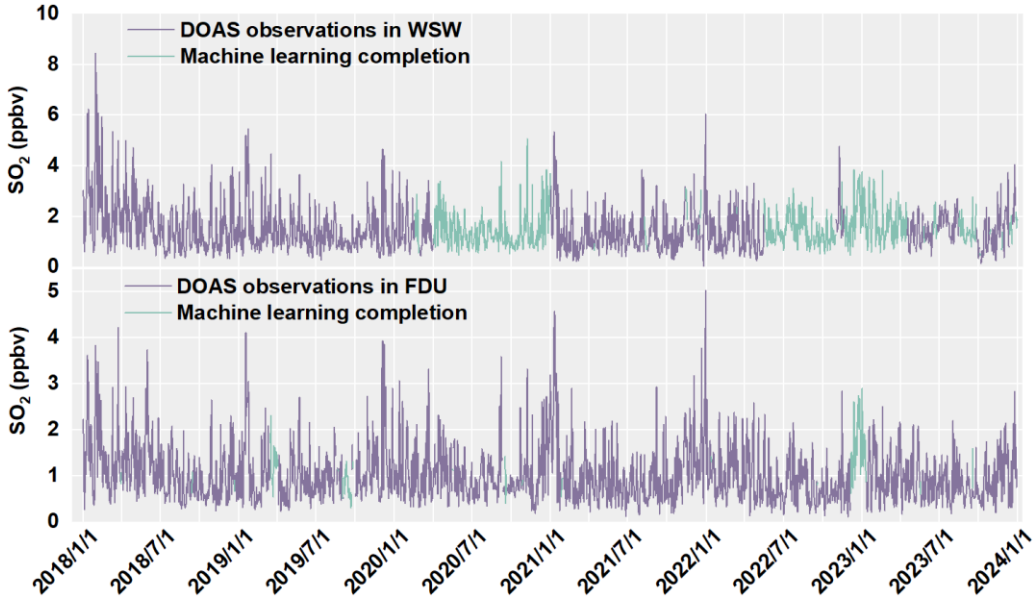

Figure S1. Time series of SO_2 for WSW and FDU complemented by DOAS observations and machine learning models.

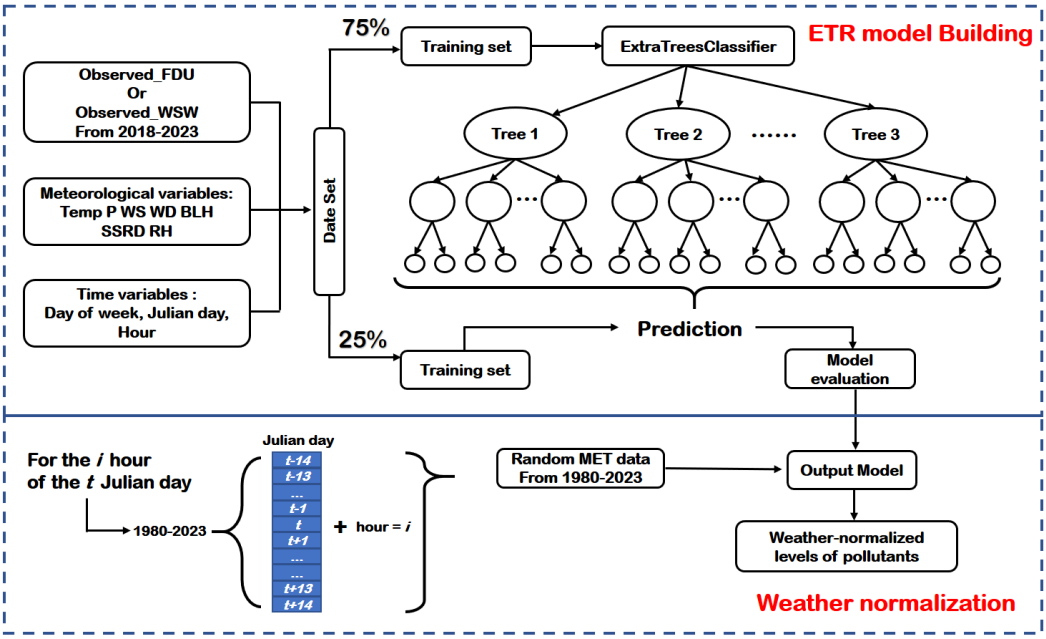

Figure S2. Deweathered model training. First train the models of Observed_WSW and Observed_FDU with temporal and meteorological feature parameters respectively for 6 years; then use the models to train the meteorological parameters for specified time periods from 1980 to 2023 and normalize the results.

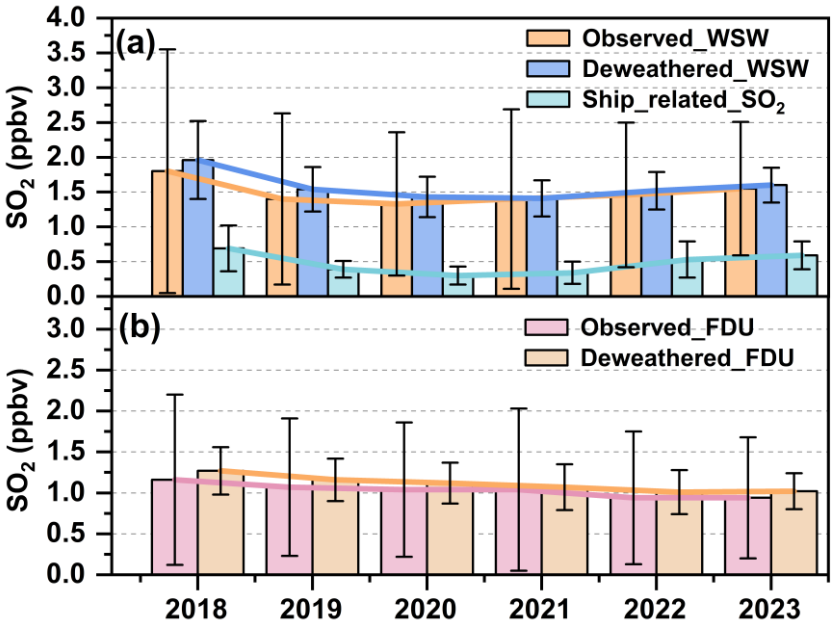

Figure S3. Yearly average SO_2 concentrations at two sites from 2018 to 2023. (a) Observed and deweathered SO_2 concentrations at the WSW site, with the contribution of ship-related SO_2. The orange bars represent observed SO_2 concentrations (Observed_WSW), the blue bars represent deweathered SO_2 (Deweathered_WSW), and the green line with stars shows ship-related SO_2. (b) Observed and deweathered SO_2 concentrations at the FDU site. The pink bars represent observed SO2 (Observed_FDU), while the

orange bars represent deweathered SO_2 (Deweathered_FDU). Error bars indicate the standard deviations of the monthly data.

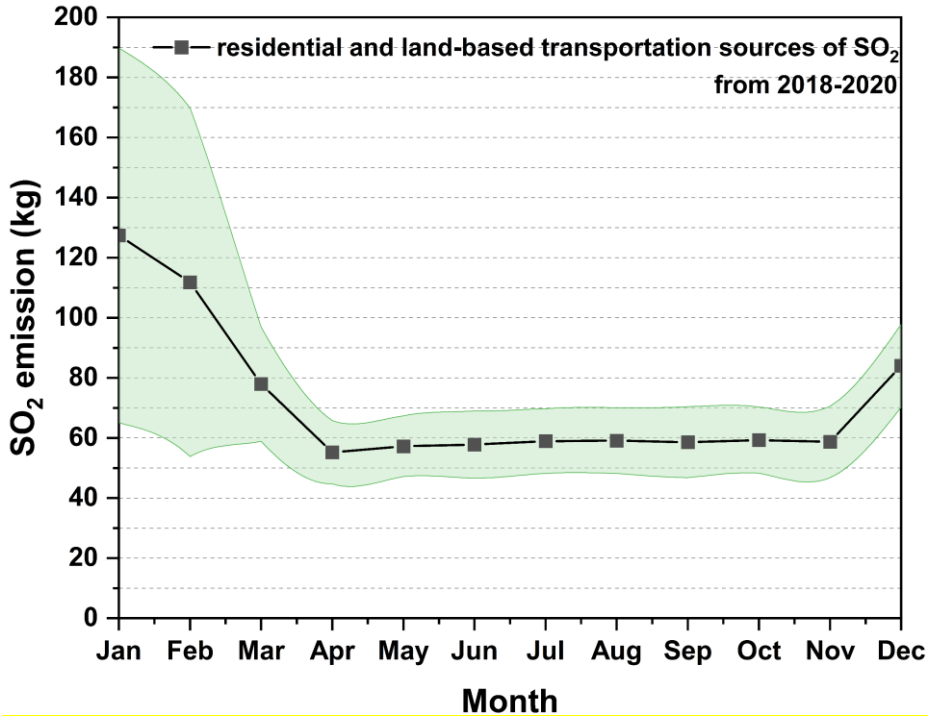

Figure S4. Monthly average values of SO_2 from residential and land-based transportation sources in Shanghai from 2018-2020 in China's Multi-Resolution Emission Inventory (MEIC).

Text S3. Matching SO_2 Peaks with Ships.

The process of matching SO_2 peaks with ships involves extracting the occurrence time of SO_2 plume signals identified by the $BEAD_S$ algorithm and searching for vessel trajectories in the cleaned AIS dataset that coincide with the plume occurrence time and intersect the light path. AIS ship track matching logic is as follows:

A straight-line equation is derived using the latitude and longitude coordinates of the DOAS emitter and the reflector as waypoints. The plume time t_{plume} is input into the system to determine, for any vessel position, whether the condition $(t_1<t_{plume}<t_2) \cap (t_2- t_1<10\text{mins}) \cap (speed_1 \neq 0) \cap (speed_2 \neq 0) \cap$ (trajectory crossing the light path) is satisfied. For any given peak, multiple vessels may potentially be matched. Assuming uniform velocity change for the vessel between t_1 and t_2. As showed in **Figure S5**.

Figure S5. Schematic Diagram of the Matching Between Ship AIS Data and SO_2-rich plume signals. With ship's positions at two locations (Location $_1$ and Location $_2$) are shown along with their respective timestamps (t_1 and t_2) and speed (Speed $_1$ and Speed $_2$). The bidirectional arrows indicate the light path of DOAS. t_{plume} indicates when the SO_2-rich plume appeared. Base map: © OpenStreetMap contributors, licensed under ODbL.

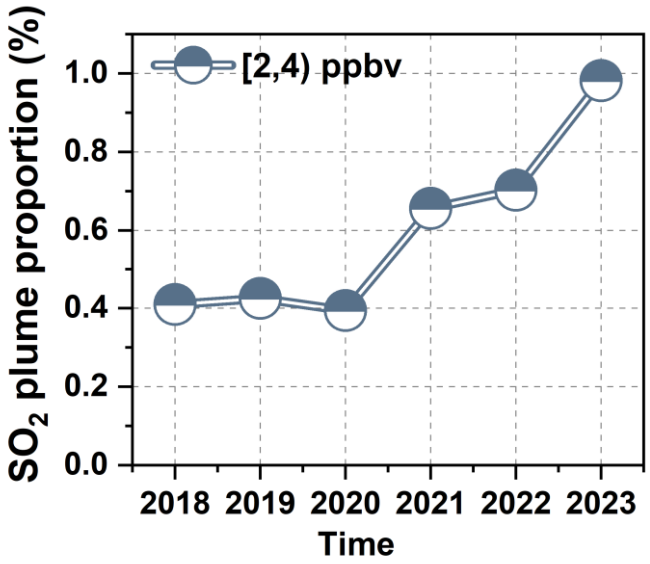

Figure S6. Annual variation in the absolute frequency of SO_2-rich plumes in the [2, 4) ppbv range from 2018 to 2023.

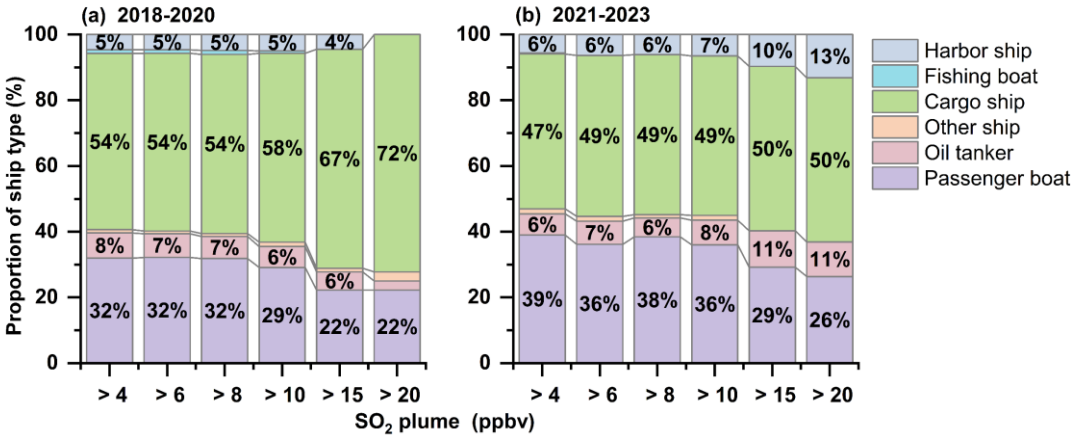

Figure S7. Proportional distribution of Fastest-Matching ship types corresponding to different peak SO_2 values during (a) the policy adjustment period (2018–2020) and (b) the policy stabilization period (2021–2023). The ship types include harbor ships, fishing boats, cargo ships, passenger boats, oil tankers, and other ships.

Text S4. Comparison Between Observational Data and AIS-Based Ship Emission Inventory

In the paragraph of this appendix, we compared Ship_related_SO_2 derived from DOAS observations with those estimated by traditional bottom-up ship emission inventories, discussed the discrepancies between the two approaches, and identified the underlying causes. AIS data provides detailed information on ship activities and is commonly used for calculating ship emission inventories on large spatiotemporal scales (Mao et al., 2020; Zou et al., 2020). Here, the ship emission inventory based on ship activities was refined (**Text S5**), resulting in an hourly emission inventory that serves as an indicator of Ship_related_SO_2 emissions within the small spatial scale of the WSW shipping channel.

The scatter plots in **Figure S8** illustrate the correlation (R^2) between ship emission inventory-based SO_2 emissions and the 14-day mean SO_2 concentrations based on observation at the WSW site. In the process of removing meteorological influences and land-based emissions, the correlation between the ship emission inventory and SO_2 concentrations progressively improves step by step. For the period from 2018 to 2020, the R^2 increases from 0.064 (Observed_SO_2) to 0.154 (Deweathered_SO_2), and further to 0.32 (Ship_related_SO_2). Similarly, for the period from 2021 to 2023, the R^2 rises from 0.043 (Observed_SO_2) to 0.163 (Deweathered_SO_2), and ultimately reaches 0.54 (Ship_related_SO_2). This trend underscores the effectiveness of the combined meteorological normalization and land-based emissions removal processes in refining our understanding of Ship_related_SO_2 contributions.

Figure S9 illustrates the 14-day mean variations of Ship_related_SO_2 concentrations and ship emission inventory in the WSW from 2018 to 2023. During the policy adjustment period (2018–2020), both the Ship_related_SO_2 and the corresponding SO_2 emissions in the inventory showed a gradual decline. If all ships had complied with the low-sulfur fuel policy, SO_2 emissions from ships would have shown a sharp decrease at the early stage of policy implementation, as illustrated in **Figure S9c**. However, due to the presence of non-compliant ships (as discussed in Sections 3.2 and 3.3), the reduction in SO_2 emissions from ships has been a gradual process, as shown in **Figure S9a**. While the consistency between Ship_related_SO_2 and the inventory improved during the policy stabilization period (2021–2023) in **Figure S8(f)**, which means that the fuel use of ships is closer to the policy requirements.

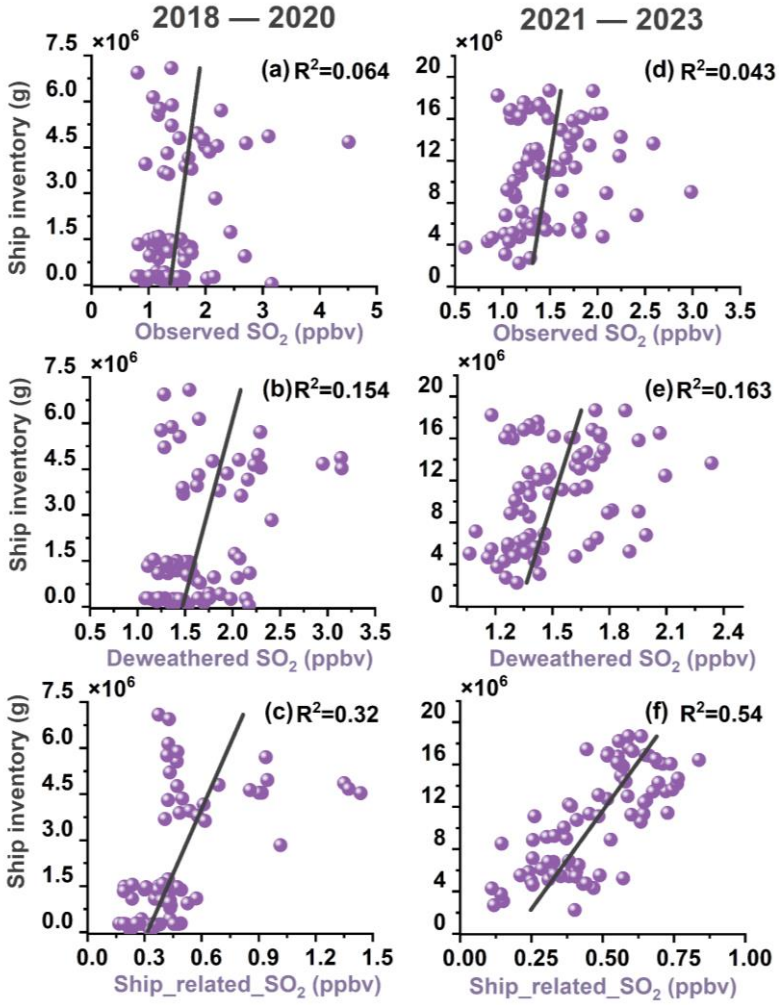

Figure S8. Correlations between 14-day mean SO_2 concentrations (x-axis) at WSW site and ship SO_2 inventory (y-axis), divided into three categories: (a, d) Observed_SO_2 concentrations, (b, e) Deweathered_SO_2 concentrations, and (c, f) Ship_related_SO_2 concentrations. (a–c) correspond to the policy adjustment period from 2018 to 2020, while panels (d–f) represent the policy stabilization period from 2021 to 2023.

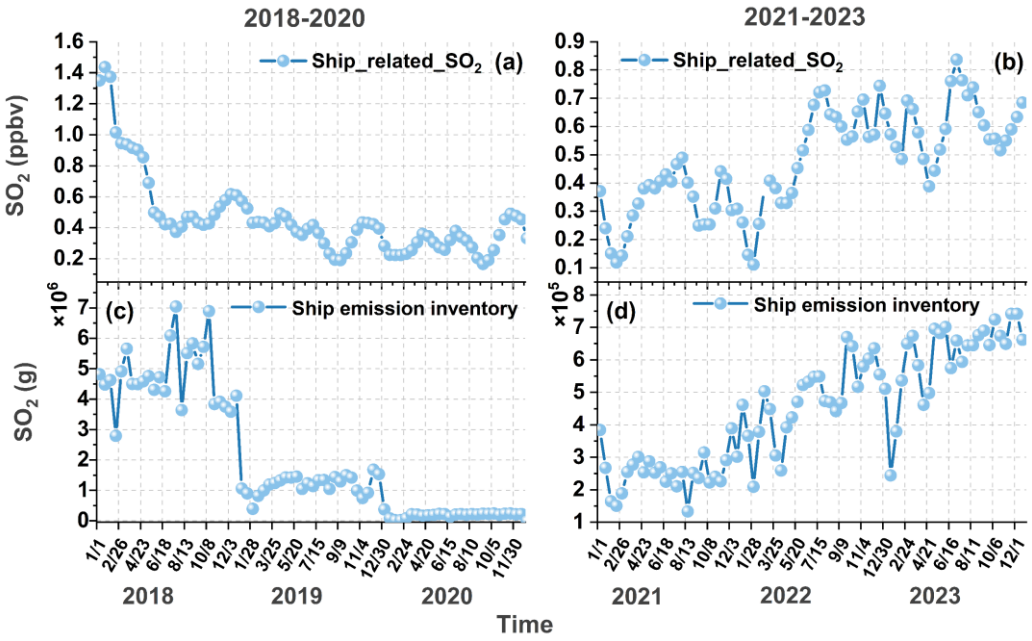

Figure S9. 14-day mean variations of Ship_related_SO_2 concentrations and emission inventory in the Wusong channel from 2018 to 2023. (a) and (b) represent the 14-day mean Ship_related_SO_2 derived from observations for 2018–2020 and 2021–2023, respectively. (c) and (d) show the corresponding 14-day mean SO_2 emissions from the ship emission inventory during the same periods.

Text S5. Calculation of ship emission inventory based on AIS.

The ship atmospheric pollutant emission inventories used in this study were calculated using a bottom-up ship emission model based on AIS data. The model was improved upon the studies by Fan et al. (2016) and Feng et al. (2019). The basic framework and specific parameters of the model are introduced as follows.

The model is primarily divided into three parts: data preprocessing, inventory calculation, and gridded output. The model has specific format requirements for the AIS data used. Since the raw AIS data contains extensive information, it is necessary to selectively extract the required information and preprocess it before inputting it into the model for further calculations. The raw AIS data includes dynamic and static information about ships. The dynamic information required by the model mainly includes the following: AIS message type (msgtype), Maritime Mobile Service Identity (MMSI), navigation status (status), current speed (speed), ship's turn direction (turn), current longitude (lon), current latitude (lat), timestamp (second), actual heading (heading), and date (day). The static information primarily includes AIS message type (msgtype), Maritime Mobile Service Identity (MMSI), International Maritime Organization (IMO) number or ship name (shipname), ship type (shiptype), distance from the positioning antenna to the bow (to_bow), distance to the stern (to_stern), distance to the port side (to_port), distance to the starboard side (to_starboard), and the current maximum static draught (draught). Before calculations, the obtained data must be classified and processed. Additionally, the ship's static information needs to be matched with corresponding basic ship information in the database.

After preprocessing the AIS data, the data is input into the calculation model one by one to compute the ship pollutant emissions. In this study, the calculation of atmospheric pollutant emissions from ships is divided into two parts: the main engine and the auxiliary engine. The calculation formula for the pollutant emissions from the main engine, E_m, is shown in Equation (2-1), while the calculation formula for the pollutant emissions from the auxiliary engine, E_a, is shown in Equation (2-2):

$$E_m = mP \times mLF \times T \times mEF \times mCF \times mLLAM \times mFCF \quad (2.1)$$

$$E_a = aP \times aLF \times T \times aEF \times aFCF \quad (2.2)$$

$$mLF = (AS/MS)^3 \quad (2.3)$$

Those parameters are:

mP/aP: Ship main engine/ auxiliary engine power, kW;

mLF/aLF: Main engine /auxiliary engine load factor;

AS: Current speed of ship, knots;

MS: Max speed of ship, knots;

mLF/aEF: Main engine/auxiliary engine emission factor, g/kWh;

mCF: Main engine control factor;

T: Time step, h;

$mLLAM$: Main engine low load adjustment factor;

$mFCF/aFCF$: Main engine/ auxiliary engine fuel control factor.

After separately calculating the pollutant emissions from the main and auxiliary engines of the ships, a gridding program is applied to aggregate the total pollutant emissions from ships within each grid area. The results are then compiled into the required ship emission inventory for subsequent analysis.

A more detailed description of the emission inventories used in this study can be found in previous articles(Fan et al., 2016; Feng et al., 2019; Yuan et al., 2023).

References.

Cheng, Y., Wang, S., Zhu, J., Guo, Y., Zhang, R., Liu, Y., et al., 2019. Surveillance of SO_2 and NO_2 from ship emissions by MAX-DOAS measurements and the implications regarding fuel sulfur content compliance. Atmos. Chem. Phys. 19 (21), 13611-13626.

Fan, Q., Zhang, Y., Ma, W., Ma, H., Feng, J., Yu, Q., et al., 2016. Spatial and Seasonal Dynamics of Ship Emissions over the Yangtze River Delta and East China Sea and Their Potential Environmental Influence. Environmental Science & Technology. 50 (3), 1322-1329.

Feng, J., Zhang, Y., Li, S., Mao, J., Patton, A.P., Zhou, Y., et al., 2019. The influence of spatiality on shipping emissions, air quality and potential human exposure in the Yangtze River Delta/Shanghai, China. Atmos. Chem. Phys. 19 (9), 6167-6183.

Friedman, J.H., 2001. Greedy function approximation: a gradient boosting machine. Ann. Stat., 1189-1232.

Gall, J., Yao, A., Razavi, N., Gool, L.V.,Lempitsky, V., 2011. Hough Forests for Object Detection, Tracking, and Action Recognition. IEEE Transactions on Pattern Analysis and Machine Intelligence. 33 (11), 2188-2202.

Guo, Y., Wang, S., Gao, S., Zhang, R., Zhu, J.,Zhou, B., 2020. Influence of ship direct emission on HONO sources in channel environment. Atmospheric Environment. 242, 117819.

Hackeling, G. (2017), *Mastering Machine Learning with scikit-learn*, Packt Publishing Ltd.

Jin, J., Ma, J., Lin, W., Zhao, H., Shaiganfar, R., Beirle, S., et al., 2016. MAX-DOAS measurements and satellite validation of tropospheric NO_2 and SO_2 vertical column densities at a rural site of North China. Atmospheric Environment. 133, 12-25.

Kurucz, R.L., 1984. Solar Flux Atlas from 296 to 1300 nm. National Solar Observatory Atlas. 1

Liu, J., Wang, S., Zhang, Y., Yan, Y., Zhu, J., Zhang, S., et al., 2024. Investigation of formaldehyde sources and its relative emission intensity in shipping channel environment. Journal of Environmental Sciences. 142, 142-154.

Mao, J., Zhang, Y., Yu, F., Chen, J., Sun, J., Wang, S., et al., 2020. Simulating the impacts of ship emissions on coastal air quality: Importance of a high-resolution emission inventory relative to cruise- and land-based observations. Science of The Total Environment. 728, 138454.

Meller, R.,Moortgat, G.K., 2000. Temperature dependence of the absorption cross sections of formaldehyde between 223 and 323 K in the wavelength range 225-375 nm. J. Geophys. Res.: Atmos. 105 (D6), 7089-7101.

Stutz, J., Kim, E., Platt, U., Bruno, P., Perrino, C.,Febo, A., 2000. UV-visible absorption cross sections of nitrous acid. J. Geophys. Res.: Atmos. 105 (D11), 14585-14592.

Vandaele, A.C., Hermans, C., Simon, P.C., Carleer, M., Colin, R., Fally, S., et al., 1998. Measurements of the NO2 absorption cross-section from 42 000 cm−1 to 10 000 cm−1 (238–1000 nm) at 220 K and 294 K. Journal of Quantitative Spectroscopy and Radiative Transfer. 59 (3), 171-184.

Voigt, S., Orphal, J., Bogumil, K.,Burrows, J., 2001a. The temperature dependence (203-293 K) of the absorption cross sections of O_3 in the 230-850 nm region measured by Fourier-transform spectroscopy. J. Photochem. Photobiol., A. 143 (1), 1-9.

Voigt, S., Orphal, J., Bogumil, K.,Burrows, J.P., 2001b. The temperature dependence (203–293 K) of the absorption cross sections of O3 in the 230–850 nm region measured by Fourier-transform spectroscopy. Journal of Photochemistry and Photobiology A: Chemistry. 143 (1), 1-9.

Voigt, S., Orphal, J.,Burrows, J.P., 2002. The temperature and pressure dependence of the absorption cross-sections of NO_2 in the 250-800 nm region measured by Fourier-transform spectroscopy. J. Photochem. Photobiol., A. 149 (1-3), 1-7.

Wang, Y., Dörner, S., Donner, S., Böhnke, S., De Smedt, I., Dickerson, R.R., et al., 2019. Vertical profiles of NO2, SO2, HONO, HCHO, CHOCHO and aerosols derived from MAX-DOAS measurements at a rural site in the central western North China Plain and their relation to emission sources and effects of regional transport. Atmos. Chem. Phys. 19 (8), 5417-5449.

Yuan, Y., Zhang, Y., Mao, J., Yu, G., Xu, K., Zhao, J., et al., 2023. Diverse changes in shipping emissions around the Western Pacific ports under the coeffect of the epidemic and fuel oil policy. Science of The Total Environment. 879, 162892.
Zou, Z., Zhao, J., Zhang, C., Zhang, Y., Yang, X., Chen, J., et al., 2020. Effects of cleaner ship fuels on air quality and implications for future policy: A case study of Chongming Ecological Island in China. Journal of Cleaner Production. 267, 122088.